PAPER

Check for updates

Study of the Fischer–Tropsch synthesis on nano-precipitated iron-based catalysts with different particle sizes

Zhonghao Han, [a] Weixin Qian,[a] Hongfang Ma,[a] Xian Wu,[a] Haitao Zhang, [a] Qiwen Sun[b] and Weiyong Ying [a]

Nano iron-based catalysts with different particle sizes were prepared by a co-precipitated method and characterized by XRD, N_2 adsorption, SEM, Mössbauer spectroscopy, XPS, H_2-TPR, CO-TPD, H_2-TPD and TGA. The CO-TPD results revealed that large particle sizes of catalysts were not conducive to the adsorption of CO, and exhibited low activity of FTS. The decrease of catalyst particle size enhanced the interaction between Fe and Mn, and promoted the CO chemical adsorption and the formation of Fe_5C_2, but the hydrogenation reaction was inhibited as confirmed by H_2-TPD. When the particle size continued to decrease, Mössbauer spectroscopy showed that $MnFe_2O_4$ appeared in the catalyst phase, which hindered the reduction of catalysts and the adsorption of feed gas. Overall, the sample FeMnSm-600 showed the highest $C_{2-4}^=$ selectivity of 33% at the highest CO conversion of 79% during the reaction conditions of 300 °C, 1.0 MPa, 12 000 mL (g h)$^{-1}$, and $H_2/CO = 2$.

1. Introduction

The increasing depletion of fossil energy resources has attracted societal awareness of environmental protection. Therefore, as an important chemical product, the production method of low-carbon olefin ($C_{2-4}^=$) has been increasingly restricted.[1] Thus, the Fischer–Tropsch synthesis (FTS) has gained more and more attention. FTS is a chemical reaction process that has been proved to be feasible to synthesize CO and H_2 into liquid fuel and gaseous hydrocarbon devoid of sulfur, nitrogen or aromatic compounds.[2] Co and Fe are common FTS catalysts. Cobalt-based catalysts are suitable for the production of liquid fuels and paraffins due to low methane selectivity and high chain growth probability.[3] Compared with Co catalysts, Fe-based catalysts are low cost, and suitable for high temperature Fischer–Tropsch syntheses (HTFT) with a wider product distribution.[4] Iron-based catalysts are mostly used for the preparation of low-carbon olefins (FTO).

Fischer–Tropsch synthesis with Fe catalysts has been a hot topic in recent decades. Pure iron catalysts have a poor effect but a promoter could significantly improve the performance of the catalyst.[5] Mn is considered to be the most common FTO

Engineering Research Center of Large Scale Reactor Engineering and Technology, Ministry of Education, State Key Laboratory of Chemical Engineering, School of Chemical Engineering, East China University of Science and Technology, Shanghai 200237, China. E-mail: zht@ecust.edu.cn; Fax: +86 21 64252192; Tel: +86 21 64252151

State Key Laboratory of Coal Liquefaction and Coal Chemical Technology, Shanghai 201203, China

promoter. Research has shown that with the addition of Mn, both the activity and olefin selectivity of FTS could be improved.[6,7] Some studies have shown that Mn can increase the stability of iron-based catalysts and prolong their service life.[8] Mn has also shown to promote the formation of iron carbide and thus increase the activity of FTS.[9] Other promoters, especially rare earth metal promoters, have been less studied. Investigations have revealed that rare earth metal promoters could restrain the hydrogenation but enhance the adsorption and dissociation of CO, promoting higher gasoline and middle fractions selectivity and obvious inhibition of both methane and wax formation.[10] It has been proved that the addition of a small amount of rare earth metals to catalysts can significantly improve the FTS performance, while excessive addition would be detrimental.[11,12]

Nano catalysts have been gradually studied in recent years due to their unique properties. Compared with traditional catalysts, the nano catalysts showed higher FTS activity and water–gas shift reaction (WGS) activity.[13] In addition, nano iron-based catalysts have been proved to achieve a higher selectivity of low olefins.[14] It is also considered that the co-precipitated iron-based catalysts would not facilitate the adsorption and the dissociation of CO and the formation of Fe_5C_2, which has been considered the active phase of FTS.[11] Park *et al.* studied the influence of the particle size of supported Fe/Al nano catalysts used in FTS.[19] It was found that the large particle catalysts contributed to the formation of C_{5+}, while the small particle catalysts were difficult to reduce, so there was a suitable particle size for FTO. It was concluded that for small particles, a dramatic increase could be observed for the surface residence

times of reversibly bonded CH_x and OH_x intermediates, whereas a sharp decrease could be observed for the CO residence time.[15] Similar results have been confirmed on the small particle catalysts in which the CO coverage decreased while the H coverage increased, which would reduce the carbon chain growth probability, leading to an increase of CH_4 selectivity.[16]

The FTS nano iron-based catalysts are usually prepared by impregnation, hydrothermal synthesis and solvothermal synthesis. However, these methods are complex in operation, high in cost and low in preparation efficiency. In our study, FeMnSm catalysts with different particle sizes were prepared by a co-precipitation method. The influence and effects of different particle sizes on the Fischer–Tropsch synthesis reaction were analyzed and discussed. All catalysts were examined by X-ray diffraction (XRD), N_2-adsorption, scanning electron microscopy (SEM), Mössbauer spectroscopy (MES), X-ray photoelectron spectroscopy (XPS), temperature programmed reduction (TPR), temperature programmed desorption (TPD) and thermogravimetric analysis (TGA). All catalysts were performed in a fixed bed reactor.

2. Experimental

2.1. Chemicals

Iron(III) nitrate nonahydrate (>99.99 wt% Shanghai Macklin Biochemical Co., Ltd), manganese nitrate (50 wt% Shanghai Macklin Biochemical Co., Ltd), samarium(III) nitrate hexahydrate (>99.99 wt% Shanghai 3A Chemical Co., Ltd) and anhydrous sodium carbonate (>99.99 wt% Shanghai Macklin Biochemical Co., Ltd) were purchased. Deionized water was used for all experiments.

2.2. Catalyst preparation

All nano iron-based catalysts were prepared by a co-precipitated method. Briefly, $Fe(NO_3)_3 \cdot 9H_2O$ (12.2 g), 50% $Mn(NO_3)_2$ (1.06 g), and $Sm(NO_3)_3 \cdot 6H_2O$ (0.13 g) were dissolved in X mL deionized water ($X = 150, 300, 600, 900,$ and 1200). Na_2CO_3 used as precipitant was prepared in a 0.2 mol L^{-1} solution and was dripped into the mixed solution at a rate of 2 mL min^{-1} until the pH value reached 8.0 ± 0.3. The whole process was kept at a high speed of stirring to avoid localized supersaturation of the solution. The stirring was continued for 0.5 h and aged for 1 h. After washing, filtration and drying, the precipitate was treated at 550 °C in air atmosphere for 3 h. Samples were labeled as FeMnSm-150, FeMnSm-300, FeMnSm-600, FeMnSm-900, and FeMnSm-1200, respectively.

2.3. Catalyst characterization

The compositions of the catalysts were measured by X-ray powder diffractometer. The XRD patterns of samples were obtained at 40 kV and 100 mA, with Cu Kα radiation ($\lambda = 0.154$ nm) and a scanning rate of 6° min^{-1} and a 2θ angle ranging from 10 to 80°.

The contents of Mn, Fe, and Sm in all fresh and reacted samples were quantified by inductively coupled plasma atomic emission spectroscopy (ICP-AES), which were performed on the Agilent 725ES instrument.

The BET surface area, pore volume, and average pore size distribution of the samples were determined by a Micromeritics ASAP 2020 automated system during N_2 physical adsorption–desorption at 77 K. Before the adsorption measurement, all samples were evacuated at 120 °C for 4 h. Specific surface areas were measured by the Brunauer–Emmett–Teller (BET) method. Pore volumes and pore sizes were measured by the Barrett–Joyner–Halenda (BJH) procedure.

Scanning electron microscopy (SEM) images were recorded using an Inspect F50 (FEI). Before each measurement, the sample was ground to below 200 mesh and a small amount of it was ultrasonically dispersed in anhydrous ethanol for 10 min.

The Mössbauer spectroscopy (MES) of catalyst samples was investigated on an MR-351 constant-acceleration Mössbauer spectrometer (FAST, Germany) at room temperature by [57]Co in a Pd matrix. The spectra were collected over 512 channels in the mirror image format. Mössbauer parameters including isomer shift (IS), quadruple splitting (QS), and hyperfine field (Hhf) were used to identify the components of the iron phase. The reacted samples were kept in nitrogen atmosphere to avoid oxidation before measurement.

X-ray photoelectron spectroscopy (XPS) measurements were performed on a VG ESCALAB 250Xi electron spectrometer equipped with a hemispherical analyzer operated in a constant pass energy mode, and an Al Kα X-ray source operated at 10 mA and 12 kV. The samples were reduced by H_2 at 350 °C for 10 h, and kept in nitrogen atmosphere to avoid oxidation before measurement.

The H_2-TPR of the fresh catalysts was carried out in a conventional atmospheric quartz flow reactor by Micromeritics Autochem 2920 apparatus with a thermal conductivity detector (TCD). About 50 mg catalysts were purged in a flow of He at 350 °C for 2 h, then cooled to 60 °C. Each sample was treated in 10% H_2/90% Ar (v/v) at a flow rate of 50 mL min^{-1}, and the reduction temperature was heated from room temperature to 800 °C at the rate of 10 °C min^{-1}.

The CO-TPD was carried out using a Micromeritics Autochem 2920 apparatus with a thermal conductivity detector (TCD). About 100 mg samples were pre-reduced in H_2 flow at 350 °C for 2 h and were cooled to 60 °C under He gas flow. Afterwards, 5% CO/95% He (v/v) were introduced into the catalyst bed for 30 min, and then the catalyst bed was purged by He flow for 60 min. Subsequently, the samples were heated up to 800 °C at a rate of 10 °C min^{-1}, while the desorbed products were detected with the TCD detector.

The H_2-TPD was carried out using a Micromeritics Autochem 2920 apparatus with a thermal conductivity detector (TCD). About 100 mg samples were pre-reduced in H_2 flow at 350 °C for 2 h and were cooled to 60 °C under He gas flow. Afterwards, H_2 were introduced into the catalyst bed for 30 min, and then the catalyst bed was purged by He flow for 60 min. Subsequently, the samples were heated up to 800 °C at a rate of 10 °C min^{-1}, while the desorbed products were detected with the TCD detector.

Thermogravimetric analysis (TGA) was carried out using a thermal analysis system (TGA-4000, PerkinElmer). The sample was heated from room temperature to 800 °C with a heating rate of 10 °C min^{-1} in air (50 mL min^{-1}).

2.4. FTS performance

The FTS performance of the catalysts was conducted in a fixed bed reactor (ID = 10 mm). The particle size of the catalysts was 60–80 mesh, and 0.3 g of catalyst sample was mixed with 0.6 g of the same particle size quartz grains. The catalysts were reduced with H$_2$ at 350 °C, 0.10 MPa, and GHSV 4000 mL (g h)$^{-1}$ for 10 h. The FTS catalyst activity tests were maintained at 300 °C, 1.0 MPa, H$_2$/CO = 2 and 12 000 mL (g h)$^{-1}$. After FTS reaction, the outlet gases CO, H$_2$, CH$_4$, *etc.*, were analyzed by an online GC Agilent 7890A with a thermal conductivity detector (TCD). The waxes were dissolved in CS$_2$ and the oils were detected off-line by GC Agilent 7890A with a flame ionization detector (FID).

3. Results and discussion

3.1. Catalysts characterization

3.1.1. Textural properties and structures of catalysts. The phase structures of the freshly calcined FeMnSm samples were examined by XRD. The patterns of all samples and Fe$_2$O$_3$ (according to the JCPDS #99-0060) are displayed in Fig. 1. Obviously, all the samples showed the characteristic peak of Fe$_2$O$_3$. From sample FeMnSm-150 to FeMnSm-1200, the diffraction peak intensity of iron oxide decreased gradually, and a broad peak with weak intensity gradually appeared at $2\theta = 22°$, which could be attributed to amorphous Fe$_2$O$_3$. Both of these indicated that the particle size of the sample decreased gradually from FeMnSm-150 to FeMnSm-1200. This is because during the preparation of catalysts, the crystals in the high concentration solution were more likely to agglomerate and form larger particles. In contrast, in the low concentration solution, the probability was small, so the catalyst particle size was small and average.

The structural properties and textures of all catalysts were characterized by N$_2$ physisorption, and the results of the N$_2$ physical adsorption–desorption isotherms for nano FeMnSm

catalysts are shown in Fig. 2. It could be found that type IV isotherms exist in all samples, which are typical for mesoporous particles. None of the five catalysts show a significant increase in N$_2$ uptake until the relative pressure (P/P_0) increased to 0.85, and raised rapidly when P/P_0 was above 0.85. Such results also revealed the existence of large macropores and mesopores.[17] Such pore structures could reduce the diffusion resistance of feed gas and product, improving the activity of catalyst in FTS. Therefore, the contact time between syngas and catalyst is shortened, which is not helpful for increasing the species concentration (–CH$_2$–).[18] These properties show that the precipitated FeMnSm nano catalysts were not beneficial to the carbon chain growth.

BET surface area, pore volume and average pore size of the fresh catalysts with different particle sizes are shown in Table 1. It can be seen that the BET results gradually increase with the increase of water content of the solution. According to Fig. 1, the pore structures of the five catalysts were similar, so it can be inferred that the lower concentration solution will be conducive to the formation of smaller particles of catalysts. When the volume of added deionized water increased from 150 to 600 mL, both samples' average pore sizes and pore volume increased. This may be due to the reduction of catalyst particle sizes and the large BET surface area. As the volume of water increased to 1200 mL, the sample average pore sizes decreased to 17.7 nm. This may be because when the catalyst particle size was too small, it was easy to form Fe$_2$MnO$_3$ and block the catalyst channels, resulting in the reduction of its pore size.[19] This will be further discussed with the H$_2$-TPR and MES results. Besides, no significant changes were observed in the pore volume, which may be due to the interaction of catalyst particle size and pore size.

As a surface-controlled process, FTS was affected by the size and shape of iron-based catalysts. SEM was carried out to study the morphology, structure and particle size of the catalysts. Fig. 3 shows the SEM images of the five catalysts. As shown in
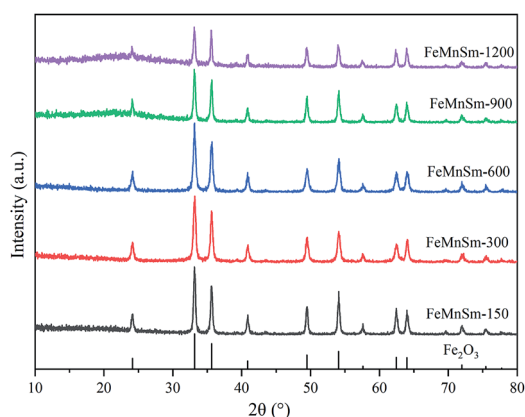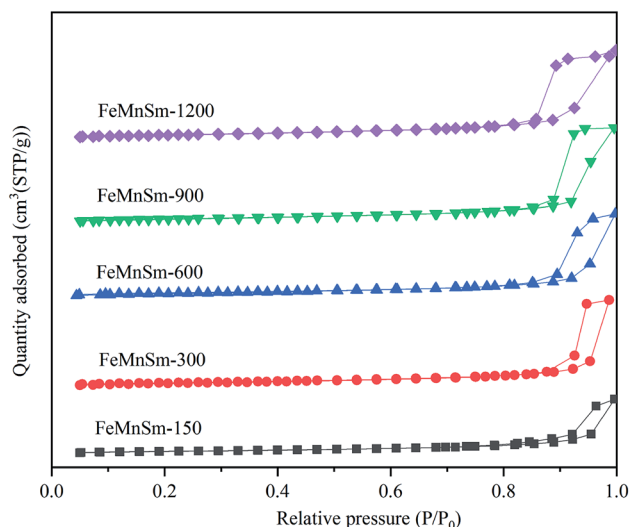

Fig. 1 XRD patterns of fresh FeMnSm nano catalysts.

Fig. 2 N$_2$ physical adsorption–desorption isotherms of the FeMnSm nano catalysts.

Table 1 Results of N_2-physisorption of the fresh FeMnSm nano catalysts

Catalyst	Fe/Mn/Sm molar ratio of sample[a]		BET surface area (m^2 g^{-1})	Pore volume (cm^3 g^{-1})	Average pore size (nm)	Particle size[b] (nm)
	Fresh	Reacted				
FeMnSm-1200	100/11/1	100/11/1	34.5	0.20	17.7	38.33
FeMnSm-900	100/10/1	100/10/1	33.2	0.21	20.9	53.56
FeMnSm-600	100/10/1	100/10/1	26.8	0.23	25.3	60.58
FeMnSm-300	100/10/1	100/10/1	22.6	0.22	22.9	67.75
FeMnSm-150	100/10/1	100/10/1	19.9	0.21	21.0	83.16

[a] Determined by ICP. [b] Determined by SEM.

Fig. 3A and B, a huge amount of Fe nanoparticles with inhomogeneous sizes were formed. Obviously, these heterogeneous particles were formed by the agglomeration of small particles. These results could be explained by the fact that the crystal growth rate was lower than the nucleation rate. When the solution concentration was high, the iron nuclei could easily contact each other. That meant new crystal nuclei formed when the crystal was not fully grown, leading to the serious agglomeration of Fe nanoparticles. In Fig. 3C–E, it could be observed that the size of iron nanoparticles gradually decreased and the particle structures were well-defined. These showed that the low concentration solution was not conducive to crystal growth, leading to the formation of small particles of catalysts.

3.1.2. Phase composition of catalysts after reaction. Mössbauer spectroscopy (MES) was used to measure the bulk iron phases in FeMnSm nano catalysts after the FTS. The MES parameter results are listed in Table 2. The superparamagnetic (spm) doublet with an IS value of approximately 0.17–0.66 mm s^{-1} could be attributed to the octahedral Fe^{3+} ion of the superparamagnetic state with small crystallites.[20] The sextets with hyperfine field (Hhf) of 458.76–490.49 kOe could be assigned to Fe_3O_4 and the sextets with hyperfine field (Hhf) of 100.07–217.26 kOe could be considered χ-Fe_5C_2.[21] In addition, the Hhf value of 426.9–433.58 kOe belongs to the oxide $M_xFe_{(3-x)}O_4$ formed by the Fe and the unknown metal M. Table 2 indicated that the samples FeMnSm-150, FeMnSm-300 and FeMnSm-600 only comprise Fe^{3+}, Fe_3O_4, and χ-Fe_5C_2 after the FTS reaction. The ratio of χ-Fe_5C_2 in the Fe species increased from 51.0 to 74.5%, as the H_2O content increased from 150 to 600 mL, while the ratio of Fe_3O_4 decreased from 42.9 to 3.5%. These results implied that in FTS, the catalyst with smaller particles were beneficial to the transformation of Fe_3O_4 to χ-Fe_5C_2. This was due to the strong chemical adsorption capacity of small particle catalysts for CO and the generation of Fe–C bonds, which will be discussed with the CO-TPD results. It is recognized that Fe_5C_2 is the active center of FTS.[22] Such results suggested that compared with FeMnSm-150, FeMnSm-600 had higher FTS activity. When the amount of water in the catalyst preparation process increased to 900 and 1200 mL respectively, a new phase $M_xFe_{(3-x)}O_4$ could be detected. According to the materials and chemical valence, the compound could be inferred as $MnFe_2O_4$, meaning that iron spinel will form when the particle size was too small. Park et al. showed that when the catalyst

particle size was too small, the interaction between Fe and other metals increased, which would lead to the formation of iron spinel.[19] In samples FeMnSm-900 and FeMnSm-1200, the content of Fe_3O_4 increased to 54.5% and 58.9%, and χ-Fe_5C_2 decreased gradually to 28.3% and 19.8%. This meant that the formation of $MnFe_2O_4$ was not conducive to the carbonization of iron and the transformation from Fe_3O_4 to χ-Fe_5C_2, which would be proved with the CO-TPD results. Notably, the contents of $MnFe_2O_4$ were 6.1% in FeMnSm-900 and 11.7% in FeMnSm-1200, but its diffraction peak was not observed in the XRD pattern, indicating that the particle sizes of $MnFe_2O_4$ were small. This could be one of the factors for the decrease of particle size shown in SEM.

3.1.3. Electronic effect. The surface electronic structure of the FeMnSm nano samples were studied by XPS measurements, as shown in Fig. 4. Two typical peaks with binding energies near 724.7 and 711.0 eV could be attributed to Fe $2p_{1/2}$ and Fe $2p_{3/2}$, respectively.[23] Fig. 4 shows that both Fe $2p_{1/2}$ and Fe $2p_{3/2}$ peaks shifted slightly toward lower binding energies with the decrease of particle size. This is because iron atoms could receive electrons from manganese atoms, and such an effect would be enhanced in catalysts with small particle sizes.[24,25]

3.1.4. Reducibility of catalysts. The reduction performance of catalysts was investigated by H_2-TPR, as shown in Fig. 5. In general, the reduction steps of iron-based catalysts were α-Fe_2O_3 → Fe_3O_4, Fe_3O_4 → FeO and FeO → α-Fe.[26] In Fig. 5, the first set of reduction peaks correspond to the process α-Fe_2O_3 → Fe_3O_4. Due to the poor stability of FeO, process Fe_3O_4 → FeO and FeO → α-Fe would be carried out at the same time, and the peaks between 570–670 °C represented that the catalyst were completely reduced to α-Fe.[27] From sample FeMnSm-150 to FeMnSm-600, the reduction peak shifted to the low temperature region. That may be because the particle size decreased and the BET surface area increased, which promoted the contact between the catalysts and H_2, and contributed to the reduction of the catalysts. However, as the catalyst particle size continued to decrease to sample FeMnSm-1200, the reduction temperature of nano iron-based particles increased significantly. From the results of Mössbauer spectroscopy, $MnFe_2O_4$ was verified to be present in samples FeMnSm-900 and FeMnSm-1200. On the one hand, the pores of the catalyst could be blocked by the formation of $MnFe_2O_4$, as confirmed in the BET study, which was not conducive to the contact between catalysts and H_2. On the other
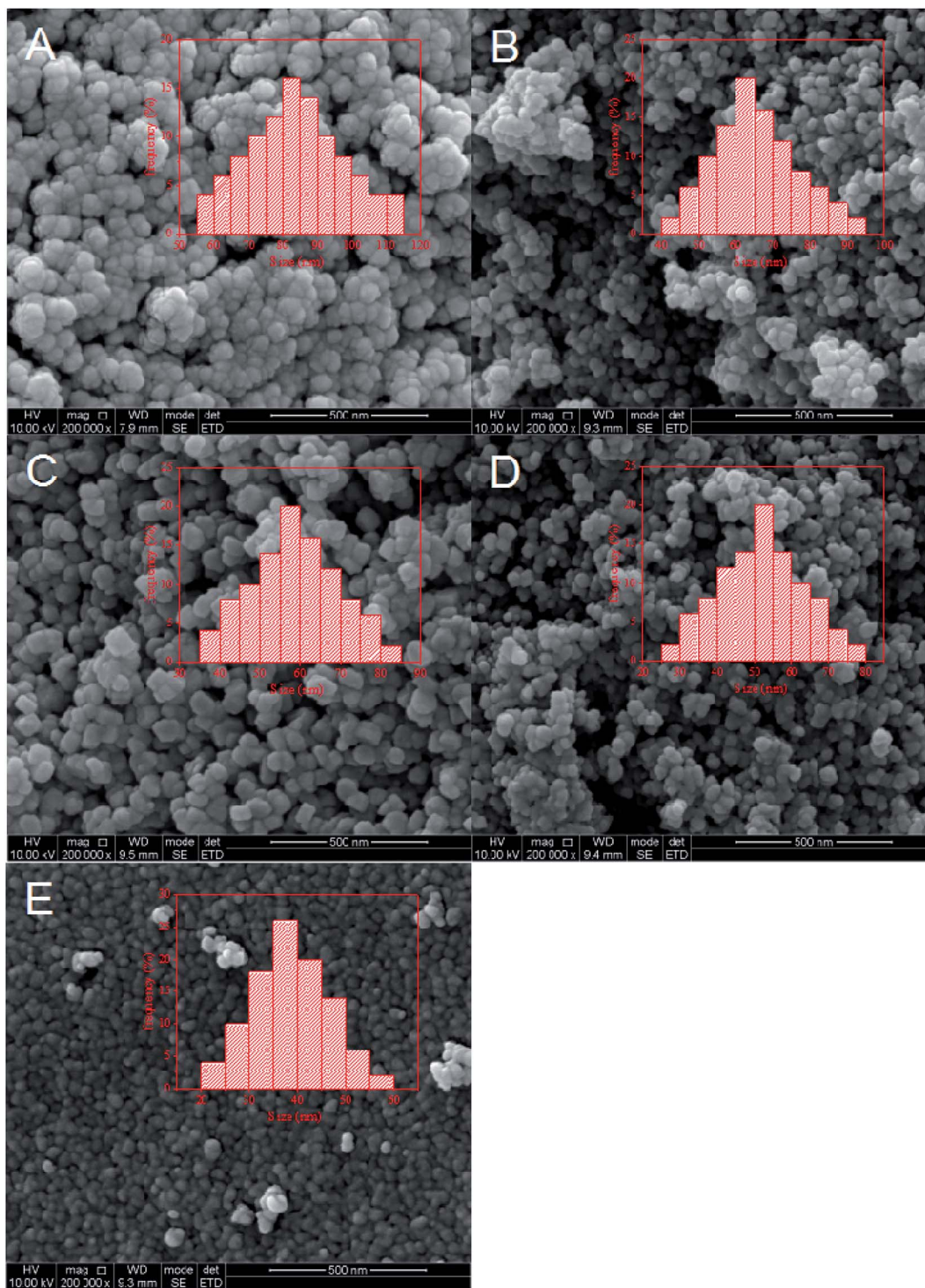
Fig. 3 SEM images of (A) FeMnSm-150; (B) FeMnSm-300; (C) FeMnSm-600; (D) FeMnSm-900; (E) FeMnSm-1200.

hand, research shows that the enhanced interaction between Fe and Mn caused by amalgamating Mn ions into the Fe lattice could limit catalyst reduction.[28,29] In addition, iron spinel was also thought to hinder the reduction of catalysts in hydrogen.[19,30]

3.1.5. Chemisorption properties of the catalysts. The adsorption morphologies and the variations in the amount of CO were analyzed by CO-TPD. The desorption peaks of all five samples are presented in Fig. 6. The desorption peaks located in the 80–200 °C range corresponded to the molecular CO adsorbed state, indicating that CO adsorption was weak.[31] The desorption peaks located near 400 °C could be attributed to the dissociative adsorption of CO, indicating CO adsorption was strong.[32] As shown in Fig. 6, in sample FeMnSm-150, FeMnSm-

Table 2 MES parameters of FeMnSm nano catalysts after reaction[a]

Catalyst	Assignment	Hhf (kOe)	IS (mm s^{-1})	QS (mm s^{-1})	$\Gamma/2$ (mm s^{-1})	Area (%)
FeMnSm-1200	Fe^{3+} (spm)		0.39	0.99	0.37	9.5
	Fe_3O_4	488.74	0.33	−0.03	0.25	33.3
		458.76	0.60	−0.03	0.29	25.6
	$M_xFe_{(3-x)}O_4$	433.58	0.70	−0.12	0.28	11.7
	χ-Fe_5C_2	216.06	0.25	−0.15	0.22	4.7
		171.80	0.23	−0.07	0.20	15.1
FeMnSm-900	Fe^{3+} (spm)		0.44	1.01	0.59	11.1
	Fe_3O_4	490.49	0.33	−0.05	0.40	28.8
		459.24	0.60	0.05	0.45	25.7
	$M_xFe_{(3-x)}O_4$	426.90	0.56	−0.34	0.28	6.1
	χ-Fe_5C_2	217.26	0.28	−0.12	0.27	7.0
		173.65	0.24	−0.04	0.40	20.1
		100.07	0.10	−0.14	0.13	1.2
FeMnSm-600	Fe^{3+} (spm)		0.36	1.03	0.32	22.0
	Fe_3O_4	485.73	0.40	−0.05	0.27	3.5
	χ-Fe_5C_2	215.13	0.25	−0.11	0.17	26.8
		183.7	0.20	0.00	0.22	32.2
		110.61	0.26	0.07	0.21	15.5
FeMnSm-150	Fe^{3+} (spm)		0.28	1.05	0.27	6.1
	Fe_3O_4	488.57	0.33	−0.01	0.22	22.1
		459.08	0.62	0.03	0.32	20.8
	χ-Fe_5C_2	216.73	0.29	−0.12	0.21	16.7
		172.68	0.24	−0.07	0.21	24.1
		102.66	0.20	0.01	0.21	10.2

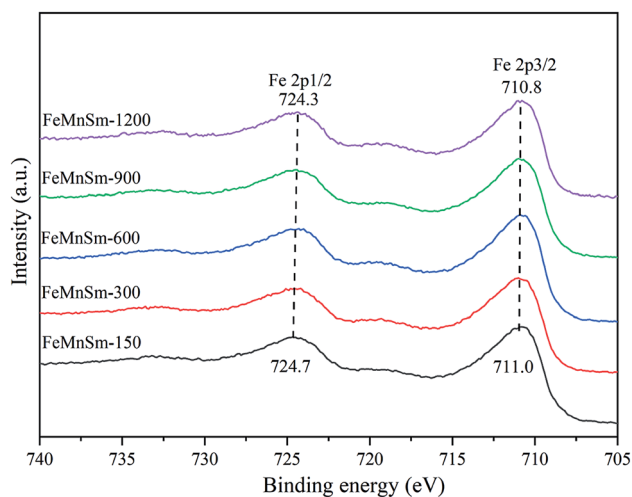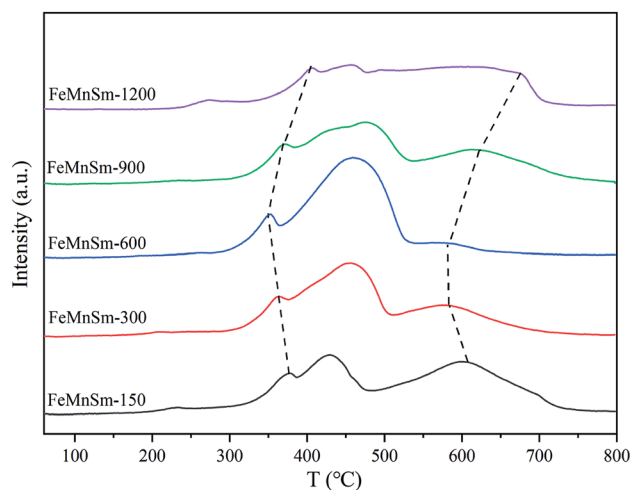[a] Reaction condition: 300 °C, $H_2/CO = 2$, 1.0 MPa, 12 000 mL (g h)$^{-1}$.

Fig. 4 XPS patterns of the FeMnSm nano catalysts.

Fig. 5 H_2-TPR patterns of the FeMnSm nano catalysts.

300 and FeMnSm-600, with the decrease of catalyst average particle size, the adsorption capacity of CO molecules decreased, while the desorption temperature and the capacity of CO dissociative adsorption increased, which meant that the catalysts with smaller particle size have a stronger CO dissociative adsorption ability. This could be due to the fact that compared with the agglomerated catalyst particles, the catalysts with good dispersion had more active sites and higher electron density on their surfaces, which contributed to the formation of Fe–C bonds. This is consistent with the Mössbauer spectroscopy and XPS results. Besides, in sample FeMnSm-900 and FeMnSm-1200, the peak intensities of dissociation desorption of CO were obviously weakened. As discussed in Mössbauer spectroscopy study, a new phase $MnFe_2O_4$ could be found in these two samples. According to the BET results, $MnFe_2O_4$ would block the pores of catalysts, which not only reduced the average pore size of catalysts, but also covered the active sites of catalysts. Furthermore, the H_2-TPR study showed that $MnFe_2O_4$ could limit the reduction of catalysts. Both results
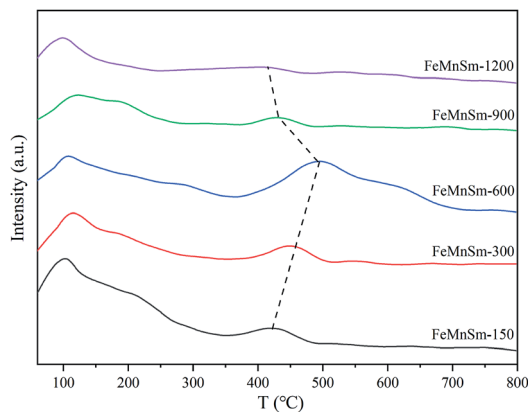
Fig. 6 CO-TPD patterns of the FeMnSm nano catalysts.

inhibited the dissociative adsorption of CO. These would prevent the formation of Fe–C bonds, resulting in less Fe_5C_2 in FTS. Such results also agree with the Mössbauer spectroscopy study.

The hydrogenation performance of the catalyst after reduction was revealed by H_2-TPD. Fig. 7 depicts the H_2 desorption peaks over all catalysts. Previous studies have showed that the H_2 desorption peaks could be divided into two types. Firstly, the H species desorbed around 100 °C tended to occupy the surface cavity or the top of the weak adsorption position, representing the weak Fe–H bond.[33] Secondly, the H species desorbed in the range of 200–300 °C could be considered as the hydrogen desorbing from the deep hole or defect locations in the surfaces of metal Fe, indicating the chemisorption of H_2.[34] It could be seen from Fig. 7 that from the aspects of temperature and intensity, no obvious difference could be observed in the weak H_2 desorption peak in the five catalysts, which meant that similar H_2 weak adsorption occurred in the five samples. In the view of strong desorption, FeMnSm-600 showed the lowest desorption temperature, corresponding to the weakest H_2 chemisorption ability. Compared with FeMnSm-150 and
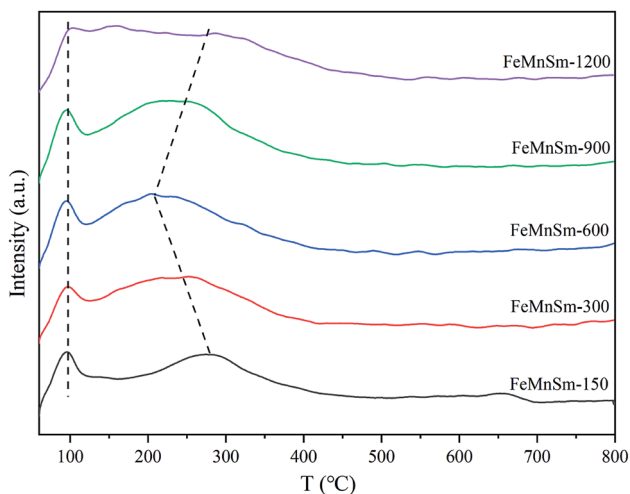
FeMnSm-300, the particle size of FeMnSm-600 was smaller and the dispersion was higher, and the electron density of the iron surface was also higher, which promoted weaker adsorption of H_2.[35] In sample FeMnSm-900 and FeMnSm-1200, both the capacity and strength of H_2 chemical adsorption increased. According to XPS, this may be due to the fact that the electron density of iron in the catalyst was lower.

3.2. Catalysts performance in FTS

The reaction data for FTS activities and product distributions of nano iron-based catalysts are listed in Table 3. The CO conversion apparently increases from 58 to 79% from sample FeMnSm-150 to FeMnSm-600. The characterization results of BET, XRD, and SEM mentioned above prove that the particle size of samples FeMnSm-150, FeMnSm-300 and FeMnSm-600 decreased gradually. The catalysts with smaller particles provided more active sites, which was helpful for the reaction of feed gas on the catalyst surface. In addition, XPS, CO-TPD and Mössbauer spectroscopy confirmed that compared with the agglomerated catalyst of FeMnSm-150, the ability of manganese donating electrons to iron was stronger in the small particle catalyst of FeMnSm-600 with good dispersion, which promoted the increase of the surface electron density of iron atoms and the adsorption of CO and the formation of Fe_5C_2, leading to a higher CO conversion. Meanwhile, according to XPS and H_2-TPD, the strong surface charge density of sample FeMnSm-600 could inhibit the adsorption of H_2, that was, weaken the hydrogenation reaction, which would not only reduce the selectivity of methane, but also oppose the conversion of olefins to alkanes, and improve the O/P of the product.[36] Furthermore, Fe_3O_4 was considered the active center of the WGS reaction. According to Mössbauer spectroscopy, FeMnSm-600 had the lowest Fe_3O_4 content, but showed the highest CO_2 selectivity, which was contrary to the widely accepted conclusions. This could be explained by a new viewpoint proposed by Liu.[37] Through the combination of theoretical study and experiments, Liu *et al.* verified that the Boudouard mechanism has a predominant effect in CO_2 formation on the active χ-Fe_5C_2 phase, but the existence of the Fe_3O_4 phase favors the reverse water-gas shift (RWGS) reaction. Our previous research also confirmed this conclusion.[24] From sample FeMnSm-600 to

Fig. 7 H_2-TPD patterns of the FeMnSm nano catalysts.

Table 3 Catalyst performance of FeMnSm nano catalysts[a]

Catalyst	CO conversion (%)	CO_2 selectivity (%)	HC distribution (%)			
			C_1	$C_{2-4}^=$	C_{2-4}^0	C_{5+}
FeMnSm-1200	35	11	20	24	19	36
FeMnSm-900	46	20	18	26	18	38
FeMnSm-600	79	46	14	33	14	39
FeMnSm-300	67	44	15	28	16	41
FeMnSm-150	58	35	17	23	18	42

[a] Reduction conditions: $T = 350$ °C, $P = 0.1$ MPa, 4000 mL (g h)$^{-1}$, H_2, TOS = 10 h. Reaction conditions: $T = 300$ °C, $P = 1.0$ MPa, 12 000 mL (g h)$^{-1}$, H_2/CO = 2.

FeMnSm-1200, the CO conversion significantly decreased to 35%. Combined with catalyst characterization, the new phase of $MnFe_2O_4$ appeared in samples FeMnSm-900 and FeMnSm-1200. It was confirmed in H_2-TPR that $MnFe_2O_4$ could inhibit the reduction of catalyst, which may be one of the reasons for the poor activities of catalysts. Besides, the formation of $MnFe_2O_4$ would not only consume iron as the active center, but also block the pores of catalysts, which were not conducive to the FTS reaction. Furthermore, compared with sample FeMnSm-600, in sample FeMnSm-900 and FeMnSm-1200, the selectivity of CH_4 and C_{2-4}^0 increases gradually, while the selectivity of C_{5+} and $C_{2-4}^=$ decreases gradually. According to BET and CO-TPD studies, the reduction of particle size would shorten the residence time of CO on the catalyst surface and weaken the chemical adsorption of CO, thus reducing the growth probability of a carbon chain. Moreover, on the basis of XPS and H_2-TPD, the lower electron density of iron atoms also provided a greater possibility for hydrogenation.

3.3. Stability performance

The results of CO conversion with TOS of different sizes of FeMnSm nano catalysts are shown in Fig. 8. As shown in Fig. 8, catalyst activities of sample FeMnSm-1200, FeMnSm-900 and FeMnSm-600 exhibited high stability. The activity of the three samples did not change significantly from the time when FTS reached the stable stage until 120 hours. However, the CO conversion of sample FeMnSm-300 decreased from 67% to 54% in 120 h. Furthermore, the activity of sample FeMnSm-150 decreased from 59% to 29%, which is most obvious. The results of the stability performance reveal the fact that smaller particles are not easily deactivated, and with the increase of catalyst particle size, deactivation will become more serious.

TG is carried out to investigate coke formation, which is considered as one of the most important reasons for the deactivation of iron-based catalysts during the Fischer–Tropsch synthesis, and the results are shown in Fig. 9. For sample FeMnSm-150, the weight loss is almost 35%, indicating obvious
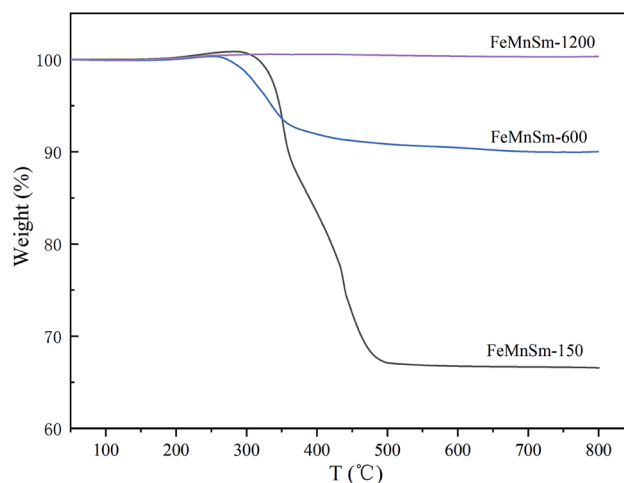

Fig. 9 TG curves of the used FeMnSm nano catalysts.

carbon deposition takes place, and this may be an important reason for its activity decrease. In contrast, the weight loss is less than 10% in FeMnSm-600, which proves that the used FeMnSm-600 sample has low carbon deposition and good stability. Meanwhile, no significant mass change was found in sample FeMnSm-1200, combined with CO-TPD results, it could be that the weak adsorption of FeMnSm-1200 to CO led to less carbon deposition. As a result, the catalyst activity remains low. The results of TG reveal that the carbon deposition of the catalyst is related to the particle size, which affects the FTS stability of the catalyst.

4. Conclusion

The nano iron-based catalysts with different particle sizes were prepared by a co-precipitated method and investigated in a fixed bed reactor. It was found that in the process of catalyst preparation, the high concentration solution more easily caused agglomeration of the catalyst particles, which would not be conducive to the adsorption of CO, and exhibited poor activity of FTS. The decrease of solution concentration promoted the dispersion of catalyst particles, enhanced the interaction between Fe and Mn, promoted the chemical adsorption of CO and the formation of Fe_5C_2. When the particle size continued to decrease, $MnFe_2O_4$ appeared in the catalyst phase, which hindered the reduction of catalysts and the adsorption of feed gas. Overall, the sample FeMnSm-600 showed the highest $C_{2-4}^=$ selectivity of 33% at the highest CO conversion of 79% during the reaction conditions of 300 °C, 1.0 MPa, 12 000 mL (g h)$^{-1}$, and $H_2/CO = 2$.

Conflicts of interest

There are no conflicts to declare.
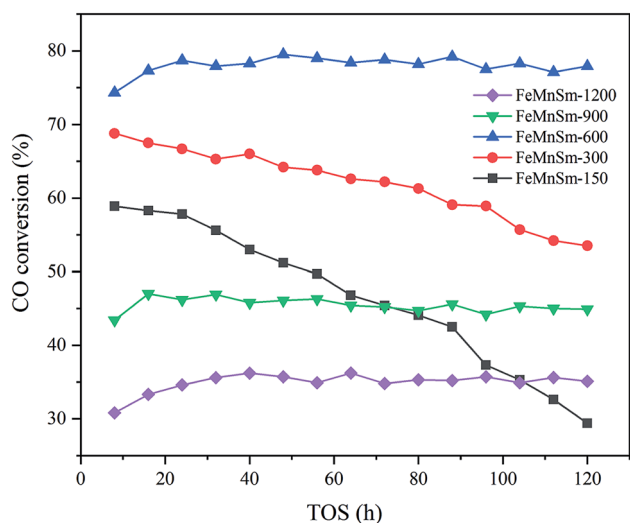
Fig. 8 CO conversion with TOS of the FeMnSm nano catalysts.

References

1 H. Schulz, *Appl. Catal., A*, 1999, **186**, 3–12.

2 G. Henrici-Olivé and S. Olive, *Angew. Chem., Int. Ed. Engl.*, 1976, **15**, 136–141.

3 E. Iglesia, *Appl. Catal., A*, 1997, **161**, 59–78.

4 R. A. Dictor and A. T. Bell, *J. Catal.*, 1986, **97**, 121–136.

5 D. B. Bukur, D. Mukesh and S. A. Patel, *Ind. Eng. Chem. Res.*, 1990, **29**, 194–204.

6 N. Lohitharn and J. G. Goodwin Jr, *J. Catal.*, 2008, **257**, 142–151.

7 Y. Ji, H. Xiang, J. Yang, Y. Xu, Y. Li and B. Zhong, *Appl. Catal., A*, 2001, **214**, 77–86.

8 Y. Yang, H. Xiang, R. Zhang, B. Zhong and Y. Li, *Catal. Today*, 2005, **106**, 170–175.

9 Y. Liu, J. Chen, J. Bao and Y. Zhang, *ACS Catal.*, 2015, **5**, 3905–3909.

10 D. Wang, X. Cheng, Z. Huang, X. Wang and S. Peng, *Appl. Catal.*, 1991, **77**, 109–122.

11 W. Han, L. Wang, Z. Li, H. Tang, Y. Li, C. Huo, G. Lan, X. Yang and H. Liu, *Appl. Catal., A*, 2019, **572**, 158–167.

12 L. Zhao, G. Liu and J. Li, *Chin. J. Catal.*, 2009, **30**, 637–642.

13 A. N. Pour, M. R. Housaindokht, S. F. Tayyari and J. Zarkesh, *J. Nat. Gas Chem.*, 2010, **19**, 284–292.

14 H. M. T. Galvis, J. H. Bitter, C. B. Khare, M. Ruitenbeek, A. I. Dugulan and K. P. de Jong, *Science*, 2012, **335**, 835–838.

15 J. Den Breejen, P. Radstake, G. Bezemer, J. Bitter, V. Frøseth, A. Holmen and K. d. de Jong, *J. Am. Chem. Soc.*, 2009, **131**, 7197–7203.

16 Y. Liu, J. Chen and Y. Zhang, *RSC Adv.*, 2015, **5**, 29002–29007.

17 F. Bertella, P. Concepción and A. Martínez, *Catal. Today*, 2017, **289**, 181–191.

18 L. Fan, K. Yokota and K. Fujimoto, *AIChE J.*, 1992, **38**, 1639–1648.

19 J. Park, Y. Lee, P. Khanna, K. Jun, J. Bae and Y. H. Kim, *J. Mol. Catal. A: Chem.*, 2010, **323**, 84–90.

20 Y. Yang, H. Xiang, Y. Xu, L. Bai and Y. Li, *Appl. Catal., A*, 2004, **266**, 181–194.

21 M. Mahmoud, H. Hamdeh, J. Ho, M. O'shea and J. Walker, *J. Magn. Magn. Mater.*, 2000, **220**, 139–146.

22 M. V. Badani and W. N. Delgass, *J. Catal.*, 1999, **187**, 506–517.

23 C. Jia, L. Sun, F. Luo, X. Han, L. J. Heyderman, Z. Yan, C. Yan, K. Zheng, Z. Zhang and M. Takano, *J. Am. Chem. Soc.*, 2008, **130**, 16968–16977.

24 X. Wu, H. Ma, H. Zhang, W. Qian, D. Liu, Q. Sun and W. Ying, *Ind. Eng. Chem. Res.*, 2019, **58**, 21350–21362.

25 H. W. Pennline, M. F. Zarochak, J. M. Stencel and J. R. Diehl, *Ind. Eng. Chem. Res.*, 1987, **26**, 595–601.

26 F. Jiang, M. Zhang, B. Liu, Y. Xu and X. Liu, *Catal. Sci. Technol.*, 2017, **7**, 1245–1265.

27 C. Zhang, Y. Yang, B. Teng, T. Li, H. Zheng, H. Xiang and Y. Li, *J. Catal.*, 2006, **237**, 405–415.

28 M. C. Ribeiro, G. Jacobs, R. Pendyala, B. H. Davis, D. C. Cronauer, A. J. Kropf and C. L. Marshall, *J. Phys. Chem. C*, 2011, **115**, 4783–4792.

29 X. Li, B. Zhong, S. Peng and Q. Wang, *Catal. Lett.*, 1994, **23**, 245–250.

30 T. Li, Y. Yang, C. Zhang, X. An, H. Wan, Z. Tao, H. Xiang, Y. Li, F. Yi and B. Xu, *Fuel*, 2007, **86**, 921–928.

31 J. Li, X. Cheng, C. Zhang, J. Wang, W. Dong, Y. Yang and Y. Li, *J. Chem. Technol. Biotechnol.*, 2017, **92**, 1472–1480.

32 J. Li, C. Zhang, X. Cheng, M. Qing, J. Xu, B. Wu, Y. Yang and Y. Li, *Appl. Catal., A*, 2013, **464**, 10–19.

33 H. Suo, S. Wang, C. Zhang, J. Xu, B. Wu, Y. Yang, H. Xiang and Y. Li, *J. Catal.*, 2012, **286**, 111–123.

34 M. Qing, Y. Yang, B. Wu, H. Wang, H. Wang, J. Xu, C. Zhang, H. Xiang and Y. Li, *Catal. Today*, 2012, **183**, 79–87.

35 D. G. Miller and M. Moskovits, *J. Phys. Chem.*, 1988, **92**, 6081–6085.

36 Y. Zhang, T. Wang, L. Ma, N. Shi, D. Zhou and X. Li, *J. Catal.*, 2017, **350**, 41–47.

37 B. Liu, W. Li, J. Zheng, Q. Lin, X. Zhang, J. Zhang, F. Jiang, Y. Xu and X. Liu, *Catal. Sci. Technol.*, 2018, **8**, 5288–5301.